Journal of Colloid and Interface Science 713 (2026) 140143

Contents lists available at ScienceDirect

Journal of Colloid And Interface Science

journal homepage: www.elsevier.com/locate/jcis

A third-generation rhodium-based nanophotosensitizer for precision photodynamic cancer therapy

Andres Machuca [a], Roberto Alvarez-Fernandez Garcia [a], Alejandro Garcia-Garcia [b], Guillermo Aragoneses-Cazorla [a], Sonia Castillo-Lluva [b], Maria Vallet-Regi [c,d], Blanca González [c,d], Estefania Garcia-Calvo [a], Jose L. Luque-Garcia [a,*]

[a] Department of Analytical Chemistry, Faculty of Chemistry, Complutense University of Madrid, 28040 Madrid, Spain
[b] Department of Biochemistry and Molecular Biology, Faculty of Chemistry, Complutense University of Madrid, 28040 Madrid, Spain
[c] Department of Chemistry in Pharmaceutical Sciences, Faculty of Pharmacy, Complutense University of Madrid, Instituto de Investigación Sanitaria Hospital 12 de Octubre (imas12), 28040 Madrid, Spain
[d] Centro de Investigación Biomédica en Red de Bioingeniería, Biomateriales y Nanomedicina (CIBER-BBN), Spain

GRAPHICAL ABSTRACT

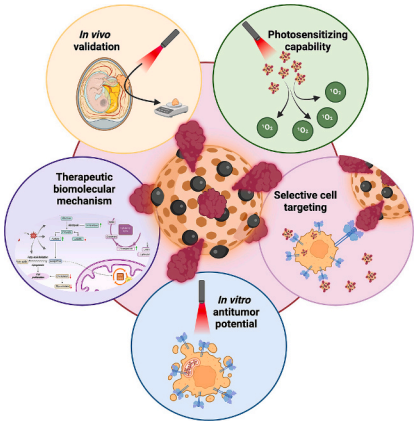

ARTICLE INFO

Keywords:
Third-generation nanophotosensitizers
Photodynamic therapy
Rhodium nanoparticles
Mesoporous silica nanoparticles
cancer therapy

ABSTRACT

Rhodium-based nanocomposites represent an unexplored class of functional materials with potential in biomedicine. Here, we present RhNPs-MSNs-Tf, a third-generation nanophotosensitizer composed of rhodium nanoparticles (RhNPs) confined within mesoporous silica nanoparticles (MSNs) and surface-modified with transferrin (Tf) to enable receptor-mediated tumor targeting. This represents the first silica-based nanocomposite integrating RhNPs for biomedical applications ever reported in literature. The hybrid structure is obtained through a robust multistep synthetic route and extensively characterized, confirming uniform RhNPs incorporation, preserved mesoporosity, colloidal stability and excellent biocompatibility. Under near-infrared (NIR) irradiation, RhNPs-MSNs-Tf efficiently generates singlet oxygen ($^1O_2$). Cellular studies demonstrate selective

* Corresponding author.
E-mail address: jlluque@ucm.es (J.L. Luque-Garcia).

https://doi.org/10.1016/j.jcis.2026.140143
Received 21 November 2025; Received in revised form 16 February 2026; Accepted 18 February 2026
Available online 21 February 2026

uptake and light-triggered cytotoxicity in cancer cells, while metabolomic analysis reveals rewiring of oxidative stress and energy metabolism pathways as underlying mechanisms. In vivo evaluation using the chicken chorioallantoic membrane (CAM) model shows significant tumor growth inhibition without apparent systemic toxicity. By combining structural precision, efficient photodynamic response and active targeting capability, RhNPs-MSNs-Tf establishes a versatile, light-activated nanoplatform. These findings highlight the promise of rhodium-based nanocomposites as next-generation functional materials for tumor-selective photodynamic therapy (PDT).

1. Introduction

Achieving selectivity remains one of the major challenges in cancer treatment. Most current clinical therapies lack the ability to distinguish between healthy and malignant cells, often leading to severe side effects and, in extreme cases, fatal outcomes. This has encouraged intense efforts in the development of alternative therapies with improved tumor-targeting capabilities. Among them, photodynamic therapy (PDT) has emerged as a promising non-invasive candidate [1–3]. PDT involves the administration of a non-toxic photosensitizer that is activated by external light irradiation, triggering the generation of reactive oxygen species (ROS) and inducing cell death in the irradiated area [4].

An ideal photosensitizer for PDT should exhibit enhanced light absorption at specific wavelengths, strong photostability, efficient reactive oxygen species (ROS) generation, minimal dark toxicity, good solubility in aqueous media, and preferential accumulation in tumor tissues. Despite the success of first- and second-generation photosensitizers in generating ROS upon light activation [5–8], they suffer from several limitations, including poor solubility in biological fluids, low tumor selectivity, and limited tissue penetration, as many of these agents, especially the first-generation photosensitizers [9], are activated by UV–vis light, which cannot effectively reach deeper tumors due the elevated molar absorptivity of biological components within this range of wavelength. Moreover, prolonged exposure to UV–vis radiation can cause phototoxicity in healthy tissues.

In this context, nanotechnology offers a powerful approach to address these limitations by enabling the design of third-generation photosensitizers based on targeted and stimuli-responsive nanomaterials [10–12]. Such nanophotosensitizers can prolong circulation time, improve bioavailability, and enable selective tumor accumulation through functionalization with targeting ligands. In addition, they can be engineered to respond to near-infrared (NIR) radiation, which not only penetrates deeper into biological tissues but exerts less phototoxicity to non-targeted areas.

Rhodium has been extensively used as a catalyst in both industrial and biomedical settings [13–15]. Its low chemical reactivity and high biocompatibility have made possible its incorporation into surgical instruments and biomedical devices [16]. While several Rh (III) complexes have shown promise as second-generation photosensitizers [17,18], the use of metallic Rh-based nanomaterials in PDT remains largely unexplored. Although some Rh-based nanomaterials have been evaluated for photothermal therapy [19,20], we previously demonstrated, for the first time, that Rh nanoparticles (RhNPs) can generate singlet oxygen under NIR laser irradiation, validating their potential as novel nanophotosensitizers [21,22]. However, free RhNPs lack tumor-targeting abilities and are challenging to functionalize directly, which could hinder their use in clinical practice.

To address this problem, we designed a novel hybrid nanosystem capable of selectively delivering RhNPs to tumor cells to enhance PDT efficacy. RhNPs were encapsulated within mesoporous silica nanoparticles (MSNs), chosen for their high surface area, tunable porosity, silanol-rich surfaces for bioconjugation, and excellent biocompatibility [23,24]. MSNs have been previously used as carriers for metallic nanoparticles in biomedical applications [25–29], but, to the best of our knowledge, this is the first report of a silica-based nanocomposite incorporating RhNPs for biomedical use. To provide active targeting, transferrin (Tf) was conjugated to the MSN surface, exploiting the overexpression of transferrin receptors (TfR) in tumor cells due to their increased iron demand [30–32]. This strategy aims to increase tumor accumulation of RhNPs [33].

Following extensive physicochemical characterization of the resulting RhNPs-MSNs-Tf nanophotosensitizer, we assessed its ability to induce photodynamic effect and cytotoxicity in HeLa cells, comparing it with MC3T3-E1 cells that exhibit significantly lower TfR expression. To further elucidate the underlying biomolecular mechanisms, we employed untargeted mass spectrometry-based metabolomics. Finally, in vivo evaluation using the chicken chorioallantoic membrane model confirmed the potential of our RhNPs-MSNs-Tf nanosystem as an active targeted third-generation nanophotosensitizer for cancer photodynamic therapy.

2. Experimental section

2.1. Materials

Rhodium trichloride (Rh 38–40%), polyvinylpyrrolidone (PVP10, Mw: 10,000 Da), ethylene glycol (99%), hexadecyltrimethylammonium bromide (CTAB, >99%), tetraethyl orthosilicate (TEOS, 98%), toluene anhydrous (99.85%), *N*-(3-dimethylaminopropyl)-*N*-ethylcarbodiimide hydrochloride (EDC·HCl, ≥97%), transferrin (≥98%), 2-(*N*-morpholino) ethanesulfonic acid monohydrate (MES, ≥99%), 4-(2-Hydroxyethyl) piperazine-1-ethanesulfonic acid (HEPES, ≥95%) and 1,2-diphenylisobenzofuran (DPBF, 97%) were purchased from Sigma Aldrich, 3-(triethoxysilyl)propyl succinic anhydride (TESPSA, 99%) was purchased from ABCR GmbH, ethyl acetate (≥99.5%) was purchased from Thermo Scientific. Dulbecco's Modified Eagle Medium (DMEM), Rosewell Park Memorial Institute (RPMI), fetal bovine serum (FBS), phosphate buffered saline (PBS), trypsin-EDTA and penicillin/streptomycin (10,000 U mL^{-1}) were purchased from Gibco®.

2.2. Synthesis of RhNPs-MSNs-Tf

53 mg of PVP10 (Mw = 10,000 Da) were dissolved in 10 mL of ethylene glycol and heated to 196 °C in a round bottom flask. Then, 10.5 mg of $RhCl_3$ were dissolved in 1 mL of H_2O and rapidly added to the previous solution. The reaction was kept under reflux at 196 °C for 1 h and formed nanoparticles were purified by centrifugation at 10,000 rpm and washing with acetone/ethanol. The solid product was dried, weighed, and resuspended in H_2O to a final concentration of 1 mg L^{-1}.

An aqueous solution (50 mL) containing 140 mg L^{-1} RhNPs and 2 mg L^{-1} CTAB in basic medium (12 mM NaOH) was heated at 80 °C for 20 min in a round bottom flask and 535 μL of TEOS were slowly added using a syringe pump at a rate of 0.107 mL min^{-1}. After addition, 2 mL of ethyl acetate were added, and the reaction was kept stirring at 80 °C for 2 h in the dark. The solid product was obtained by centrifugation at 10,000 rpm for 15 min, washed 3 times with absolute ethanol (EtOH) and dried at room temperature before further functionalization.

Surface modification of RhNPs-MSNs with carboxylic acid groups was accomplished by reaction with 3-(triethoxysilyl)propyl succinic anhydride (TESPSA). The required amount of TESPSA was calculated to achieve a maximum coverage of the total external surface of the nanomaterial. Pore surfactant containing material was used for

functionalization and, therefore, a quarter of the specific surface area of the surfactant-free material (964.0 $m^2\ g^{-1}$) and a molar ratio of one R-Si $(OEt)_3$ reacting with three Si-OH groups were considered for calculations. Briefly, 240 mg of RhNPs-MSNs were dried under vacuum at 80 °C for 3 h and dispersed in 15 mL of dry toluene in a three-necked round bottom flask under N_2 atmosphere. Then, a solution of 45 mg TESPSA in dry toluene was carefully added and reacted overnight at 100 °C under N_2 atmosphere. Solid was obtained by centrifugation, washed with absolute ethanol twice and resuspended in 150 mL of 10 g L^{-1} NH_4NO_3 in 95% EtOH / 5% H_2O for CTAB extraction. The extraction was performed at 80 °C for 3 h and repeated overnight before centrifugation. Solid material was obtained by centrifugation and washed twice with absolute EtOH before drying.

Prior to the anchoring of transferrin to the nanosystem, surface acid groups were activated using an EDC·HCl solution for 3 h (10 equiv. per nominal —COOH group). Activated RhNPs-MSNs-COOH were resuspended in 50 mM MES buffer at pH 6, and a solution of transferrin containing 1.4×10^{-3} mol of protein per nominal —COOH group in MES buffer was added dropwise and reacted overnight at room temperature. The final product was obtained by centrifugation, washed 6 times with H_2O (HPLC grade), dried at RT and stored at 4 °C.

2.3. Physicochemical characterization of the nanomaterials

Physicochemical characterization of the synthesized nanosystem as well as the intermediates was performed using transmission electron microscopy (TEM), energy dispersive X-ray spectroscopy (EDS), dynamic light scattering (DLS) and electrophoretic mobility to calculate zeta potential (ζ), attenuated total reflectance Fourier transform infrared spectroscopy (ATR-FTIR), thermogravimetric and differential thermal analysis (TGA and DTA), chemical microanalysis, X-ray diffraction (XRD) and nitrogen adsorption-desorption.

Transmission electron microscopy (TEM) and energy dispersive X-ray spectroscopy (EDS) were performed on a JEOL JEM 1400 PLUS instrument operating at 120 kV (JEOL Ltd., Tokyo, Japan). Samples were dispersed in EtOH followed by sonication in a water ultrasound bath and one drop of the suspension was deposited over a carbon-coated copper grid (grid size 200 mesh) and let dry at room temperature before imaging. Hydrodynamic particle size and electrophoretic mobility (ζ-potential) were measured on a Zetasizer Nano ZS (Malvern Instruments Ltd., UK) equipped with a 633 nm laser. For DLS measurements, approximately 1 mg of sample was resuspended in 4 mL water, sonicated until no aggregates were visible and 1 mL of this suspension was transferred to a DTS1070 disposable folded capillary cell. Each sample was measured on a quintuplicate basis and data are presented as mean ± SD. Fourier transform infrared spectroscopy was carried out using a Thermo Nicolet Nexus infrared spectrometer equipped with a Goldengate attenuated total reflectance device (ATR). IR spectra were obtained between 4000 and 400 cm^{-1}. Differential thermal analysis (DTA) and thermogravimetric analysis (TGA) were performed on a Perkin Elmer Pyris Diamond TG/DTA analyzer (Perkin Elmer, CA, USA) to determine the total organic content of the materials. For TGA measurements, approximately 5 mg of sample ($n = 3$) were placed in a platinum crucible applying 5 °C min^{-1} heating ramps from RT to 800 °C under an airflow rate of 100 mL min^{-1}. Chemical microanalyses for carbon, hydrogen, nitrogen, and sulfur content determination were performed using a Perkin Elmer 2400 CHN and LECO CHNS-932 thermoanalyzers ($n = 3$). Low-angle X-Ray diffraction (XRD) patterns were obtained from powder samples on a Phillips X'Pert PRO MPD diffractometer with Bragg-Brentano geometry operating at Cu Kα (1.5406 Å). Low-angle XRD diffractograms were collected in the 2θ range between 0.6° and 8° with a step size of 0.02° and counting time of 5 s per step. Nitrogen adsorption isotherms were obtained on a Micromeritics 3Flex Surface Characterization Analyzer. Briefly, around 30 mg of sample were placed on each sample tube and subjected to a degas process under mild heating conditions at 40 °C and high vacuum for 24 h to eliminate any humidity present on the surface of the nanomaterials. Then, degassed sample tubes were transferred to the analyzer to obtain the nitrogen adsorption isotherms. Specific surface area and pore diameter were calculated for each material from experimental isotherms by using the Brunauer-Emmett-Teller (BET) equation and Barrett-Joyner-Halenda (BJH) method, respectively. Reported values are subject to a standard instrumental error of 2%, as specified by the manufacturer for high-surface-area materials.

2.4. Singlet oxygen measurements

The photodynamic responses of RhNPs-MSNs-Tf and MSNs-Tf were evaluated using DPBF as molecular probe for singlet oxygen generation upon light excitation. Briefly, a suspension of either RhNPs-MSNs-Tf or MSNs-Tf was prepared containing a fixed concentration of 60 μM DPBF probe and exposed to 800 nm NIR laser for 10 min at 2.5 W cm^{-2}. Absorbance of the DPBF probe was measured at 415 nm.

2.5. Selective internalization

Aiming to study the selectivity of the new hybrid nanosystem toward TfR-expressing cells, an ICP-MS based assay was performed to quantify the Rh content on TfR-overexpressing (HeLa) and non-overexpressing (MC3T3E1) cells after exposure to different materials. Briefly, 1.5×10^6 cells were seeded in P100 plates, incubated for 24 h and exposed to 20 mg L^{-1} of either RhNPs-MSNs or RhNPs-MSNs-Tf for another 24 h. Then, cells were thoroughly washed with PBS several times, collected by trypsinization, and counted for further normalization. Cell suspensions were centrifuged and whole pellets were digested by boiling on H_2SO_4 until complete evaporation. Finally, samples were reconstituted in 1% HNO_3 and Rh content was analyzed by ICP-MS on a Bruker Aurora Elite instrument equipped with a quadrupole mass analyzer. A total of 5 replicates were analyzed per condition.

2.6. Intracellular localization

Intracellular localization of RhNPs-MSNs-Tf was performed using transmission electron microscopy (TEM). HeLa cells were exposed to 20 mg L^{-1} of the nanosystem for 24 h. Then, cells were harvested and incubated with 2.5% glutaraldehyde 4% p-formaldehyde in PBS for 4 h at 4 °C for protein fixation, and with 1% osmium tetroxide solution for 1 h at room temperature for lipid fixation and contrasting. Then, cells were dehydrated by incubating for 15 min with increasing concentrations of acetone in water from 30 to 100%. Similarly, cells were then embedded in epoxy resin by incubation with increasing concentrations of resin in acetone, from 25 to 100%, and finally heated at 70 °C for 72 h for complete resin polymerization. Samples were then sliced on an ultramicrotome, stained with lead citrate, and mounted for TEM examination on a JEOL JEM 1400 PLUS.

2.7. Trypan blue exclusion assay

The cytotoxicity of both the complete nanosystem (RhNPs-MSNs-Tf) and the vehicle (MSNs-Tf) on HeLa cells were evaluated with and without NIR irradiation by a live-dead trypan blue staining protocol. Briefly, cells were seeded on P96 plates at a rate of 2.5×10^3 cells per well and incubated for 24 h. Then, cells were exposed to different concentrations of either MSNs-Tf or RhNPs-MSNs-Tf for 24 h. After that time, cells were washed with PBS to remove non-internalized nanoparticles and fresh media was added; then, the NIR group was irradiated as previously described. After photodynamic treatment, cells were incubated for an additional 48 h, harvested by trypsinization, and stained with trypan blue (1:1) for 15 min for visual inspection under phase-contrast microscopy. A total of 5 replicates were prepared for each condition. Statistical analysis was performed by multiple comparison of means using ANOVA and Bonferroni post-test.

2.8. Untargeted metabolomics

To evaluate the impact of the photodynamic treatment and decipher the mechanisms that induce cell death, an untargeted metabolomic assay was performed using high-resolution gas chromatography coupled to mass spectrometry (GC–MS).

After cell exposure to RhNPs-MSNs-Tf-based PDT, metabolites were extracted following a two-phase liquid extraction protocol. First, cells were washed twice with 0.9% NaCl and chilled methanol (MeOH, −20 °C) and cold H_2O (4 °C) were added at 1:1 ratio. Cells were collected by scratching the plate surface and transferred to an Eppendorf vial, then the same volume of $CHCl_3$ was added. Complete cell lysis was achieved by probe-assisted ultrasound disruption (20 pulses, 30% amplitude, 2 s ON/5 s OFF) over ice. After extraction, polar and non-polar phases were separated by centrifugation at 16,000*g* for 5 min, transferred to separate glass GC vials adding 4-hydroxy butyric acid as an internal standard and evaporated to dryness under N_2 stream. The protein precipitate interphase was redissolved in 6 M urea/2 M thiourea/20 mM HEPES pH 8.0 buffer and used for total protein quantification for further sample normalization. A total of 7 replicates were prepared for each condition for statistical significance. For this experiment, HeLa cells cultured in DMEM supplemented with 10% FBS and not exposed to any nanomaterial were used as controls.

Metabolites were derivatized prior to GC–MS analysis following a two-step derivatization protocol. First, dried extracts were reconstituted in 30 µL of 40 mg mL^{-1} methoxyamine in pyridine and incubated at 37 °C and 500 rpm for 90 min. After that, 60 µL of 1% trimethylchlorosilane (TMCS) in *N,O*-bis(trimethylsilyl)trifluoroacetamide (BSTFA) were added and incubated at 60 °C and 500 rpm for 60 min. Samples were then filtered through 0.22 µm nylon and transferred to glass inserts for GC–MS analysis.

Samples were analyzed in a gas chromatograph (7890 A, Agilent, Santa Clara, CA, USA) using a ZB-5MS plus capillary column (30 m × 0.25 mm × 0.25 m, Phenomenex, Torrance, CA, USA) and 1 mL min^{-1} He as a carrier gas. Two microliters of sample were injected in split mode (1:10 split ratio). The inlet temperature was set at 270 °C and the oven temperature gradient was set from 60 °C to 325 °C, with a total running time of 50 min. The GC was coupled to a time-of-flight (TOF) high-resolution mass spectrometer (GCT premier Micromass, Waters, Milford, MA, USA), using an electron ionization (EI) source, and a scan mass range from 50 to 800 *m/z*. Chromatograms were obtained in total ion current (TIC) mode. The mass spectrometer was tuned and calibrated for mass resolution and mass accuracy daily using authenticated reference standards. Process coefficients of variation involving instrument performance, chromatography and mass calibration were checked to ensure quality. Ultrapure MS-quality water blanks and solvent blanks were also included in the analyses and used to assess the process contribution to signals and for the identification of potential sources of contamination.

Chromatographic data were analyzed with Mass Lynx software and metabolite identification was assessed using the National Institute of Standards and Technology (NIST) database with a Reverse Match Factor (Rmatch) threshold of 700 for unequivocal identification based on MS spectra. Peak areas for each identified metabolite were normalized using both internal standard peak area and total protein content of each replicate. A calculated fold change value (R_M) was described as the quotient of normalized areas of the same metabolite in both treated and control samples.

Statistical analysis was performed by using Metaboanalyst 6.0. Only metabolites that were present in >50% of replicates with an RSD < 20% were considered. Prior to the multivariate statistical analysis, and to minimize possible differences between samples, data were scaled considering the mean-centered and divided by the range of each variable. Data were explored and modelled by Principal Component Analysis (PCA) and Two-tailed Student's *t*-test, at a 95% confidence level was used as univariate statistical analysis to compare metabolite peak areas from both experimental conditions (*p*-value <0.05 was considered as statistically significant) ($n = 7$).

2.9. In vivo chicken chorioallantoic membrane assay

To evaluate the potential of the RhNPs-MSNs-Tf nanosystem-based photodynamic treatment in an in vivo model, a chicken embryo model was employed. Fertilized eggs were purchased from a local distributor and incubated on an automatic egg incubator at 37 °C and 60% humidity, with automatic rotation every 1.5 h. On day 7, T47D cells were seeded on P100 plates, incubated for 24 h and exposed to 20 mg L^{-1} of the RhNPs-MSNs-Tf nanosystem for another 24 h. On day 10 of embryo development, a window of 1 cm^2 was opened on the egg shell under aseptic conditions, and 1×10^6 cells were inoculated directly over the chorioallantoic membrane on each egg, using a 1:1 mixture of cell suspension in PBS and matrigel. A sterilized silicone O-ring was placed carefully over the membrane before inoculation to avoid cell spreading. Eggs were then incubated without rotation for 3 days before photodynamic treatment to achieve successful cell engrafting and tumor development. NIR conditions used were the same as previously mentioned for in vitro assays, with an irradiation time of 10 min per egg. On day 17 post-fertilization, eggs were carefully opened, embryos were euthanized, and tumors were extracted for size and weight inspection. Statistical significance was assessed based on mean multiple comparisons between conditions using ordinary one-way analysis of variance (ANOVA) test. All CAM experiments were performed before embryonic day 17 and therefore did not require ethical approval according to EU Directive 2010/63/EU.

3. Results and discussion

3.1. Synthesis and physicochemical characterization of the nanomaterial

We synthesized the Rh-based nanophotosensitizer (RhNPs-MSNs-Tf) through a multistep synthetic route outlined in Fig. 1a. Initially, rhodium nanoparticles (RhNPs) were prepared via a polyol reduction method [21,34,35]. Transmission electron microscopy (TEM) analysis (Fig. 1b) confirmed the formation of uniformly sized, irregularly shaped RhNPs with diameters ranging from 4 to 5 nm. X-ray diffraction (XRD) analysis (**Fig. S1**) revealed broadened peaks corresponding to metallic Rh, consistent with the nanoscale dimensions of the particles.

Subsequently, mesoporous silica nanoparticles (MSNs) were synthesized in situ around the RhNPs by a modified Stöber method, employing cetyltrimethylammonium bromide (CTAB) as a structure-directing agent, and tetraethyl orthosilicate (TEOS) as the silica precursor [36]. The addition of ethyl acetate after TEOS incorporation helped regulate nanoparticle morphology during the sol-gel process [37].

Surface functionalization with carboxylic acid groups was achieved via post-synthetic grafting of 3-(triethoxysilyl)propyl succinic anhydride (TESPSA) under anhydrous conditions. Upon surfactant extraction, hydrolysis and ring opening of the succinic anhydride led to the generation of carboxyl groups on the MSN surface. Transferrin (Tf) was then covalently anchored through carbodiimide-mediated coupling, enabling amide bond formation between surface-exposed —COOH groups and lysine residues of the protein [25].

Morphological analysis by TEM revealed homogeneous RhNPs-MSNs with quasi spherical morphology and no visible aggregation. (Fig. 1c, d, and **S2**). The mesoporous structure remained intact after each functionalization step (Figs. S2a-b, and S3c), with no significant morphological changes. High magnification micrographs showed ordered two-dimensional (2D) hexagonal channels and electron-dense RhNPs (~5 nm) embedded within the silica matrix (Fig. 1c). Notably, no free RhNPs were detected, indicating effective incorporation within the silica matrix. Dynamic light scattering (DLS) measurements confirmed monodisperse hydrodynamic sizes centered around 150 nm throughout the synthetic sequence (Figs. 1e and **S3d-f**), and demonstrated that RhNPs-

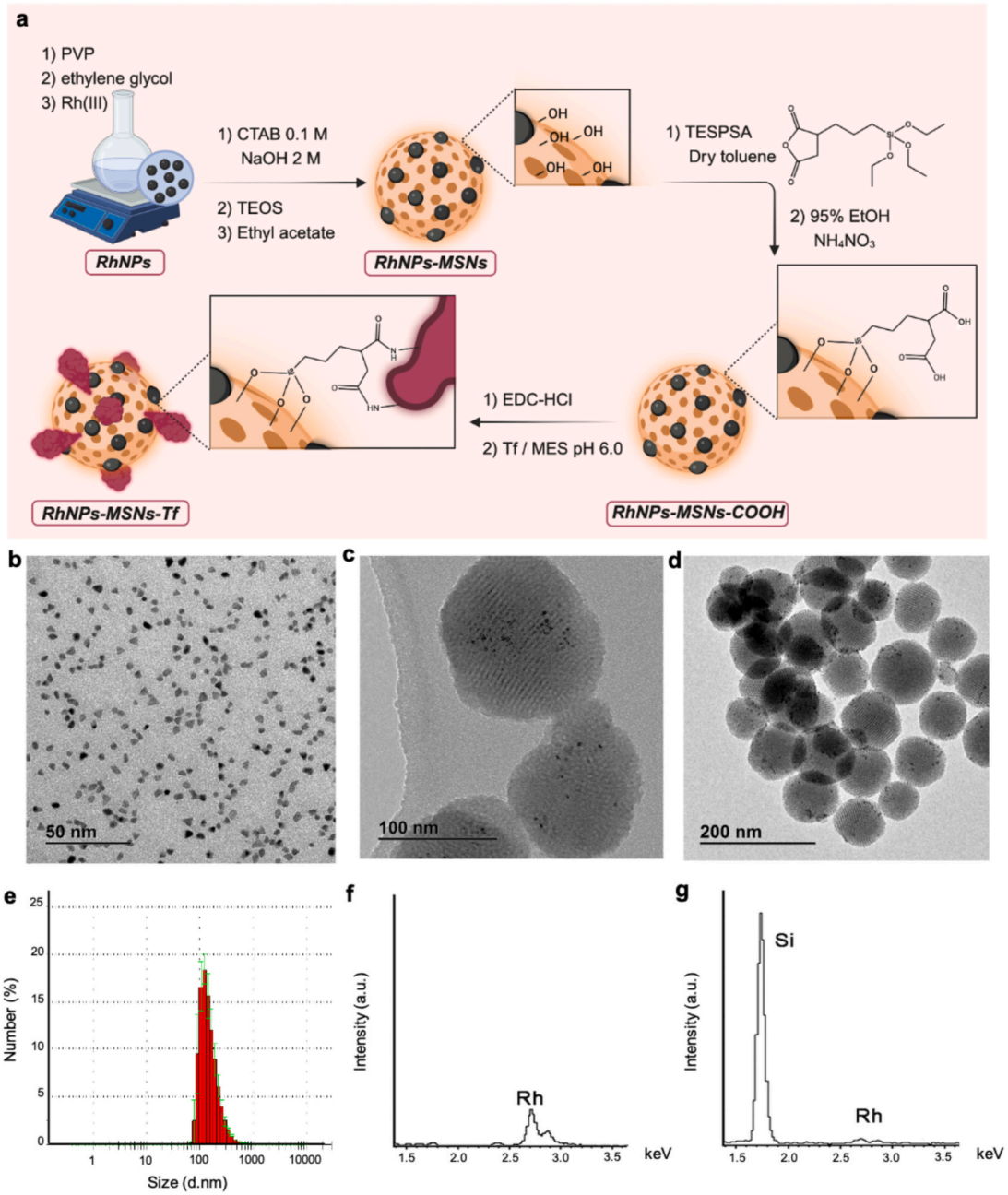

Fig. 1. (a) Schematic illustration of the synthetic route for the RhNPs-MSNs-Tf nanophotosensitizer. (b) TEM micrograph of RhNPs synthesized via the polyol reduction method. (c) High-magnification TEM micrograph revealing embedded RhNPs and the mesoporous structure of RhNPs-MSNs-Tf. (d) TEM micrograph showing quasi-spherical morphology of RhNPs-MSNs-Tf. (e) Hydrodynamic size distribution of RhNPs-MSNs-Tf determined by DLS ($n = 5$). (f) EDS spectra of the initial RhNPs. (g) EDS spectra of the final material RhNPs-MSNs-Tf.

MSNs-Tf remains colloidally stable in different media, including water, PBS and DMEM supplemented with 10% FBS, without evidence of time-dependent aggregation in PBS between 0 and 48 h (**Fig. S4**). Elemental analysis by energy-dispersive X-ray spectroscopy (EDS) confirmed the presence of Rh in both the initial and final materials (Fig. 1**f** and **g**), with an estimated atomic composition of 2% Rh and 98% Si.

Low-angle XRD patterns (**Fig. S3j**) exhibited a broad diffraction peak near 2.1°, corresponding the more intense reflection peak (10) characteristic of the highly ordered *P6mm* hexagonal mesoporous symmetry of MCM-41 materials [38], with lattice spacing mean values of around 4.2 nm. Unexpectedly, higher-order reflections (11) and (20) were not observed in the diffractogram, likely due to minor structural distortions introduced by RhNPs. However, TEM micrographs (**Figs. S2** and **S3a,b** and **c**) confirmed the presence of ordered 2D hexagonal mesostructures in all three materials.

Surface functionalization was further corroborated by ATR-FTIR spectroscopy (Fig. 2a). All samples exhibited characteristics silica bands: asymmetric Si-O-Si stretching at ~1050 cm^{-1}, Si—OH stretching at ~975 cm^{-1}, symmetric Si—O—Si stretching at ~800 cm^{-1}, and the Si—O—Si deformation mode at ~450 cm^{-1}. In the 1850–1400 cm^{-1} region, RhNPs-MSNs showed a broad band at 1625 cm^{-1}, attributed to the bending band of adsorbed water. Upon carboxylation, a distinct C═O narrow stretching band appeared at 1710 cm^{-1}, which disappeared after Tf conjugation. Instead, two new bands at 1750 and 1525 cm^{-1}, corresponding to amide ν(C═O) stretching and δ(NH) bending, respectively, confirmed successful covalent anchorage of Tf.

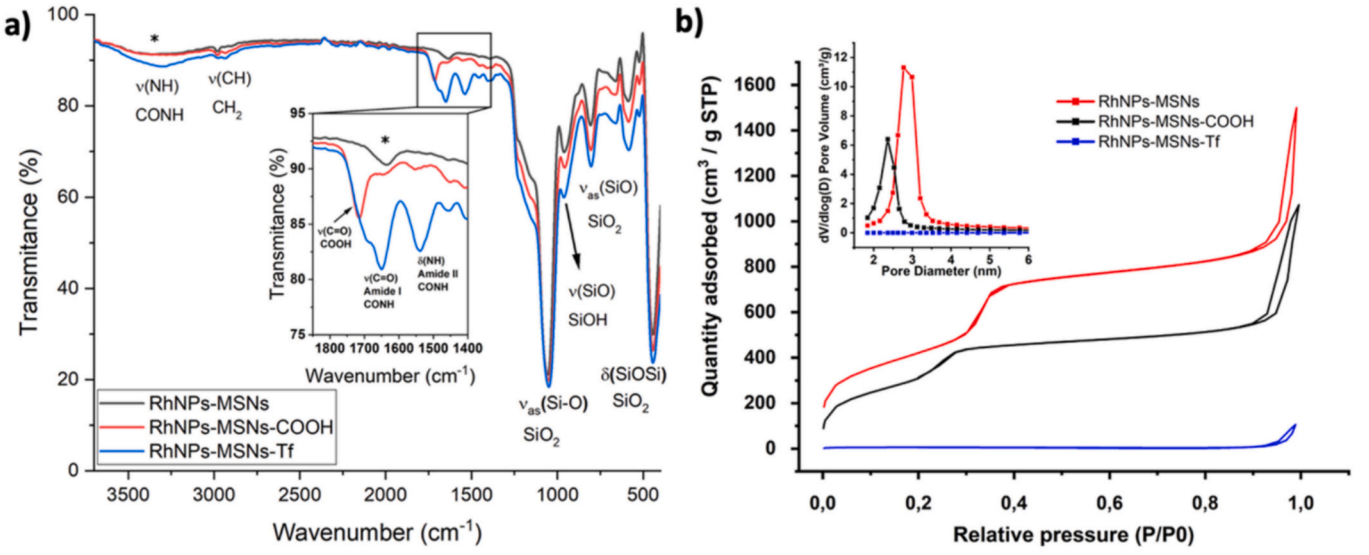

c)

Material	Hydrodynamic size (nm)	ζ-Potential (mV)	S_{BET} ($m^2\ g^{-1}$)	C constant	D_P (nm)	V_T ($cm^3\ g^{-1}$)	Org. Content [e] (wt %)	%C	%N	%S
RhNPs-MSNs	120 ± 40	-12 ± 8	964 ± 11 [a]	66 [b]	2.8	0.826	5.3 ± 0.2	5.3 ± 0.3	0.29 ± 0.07	-
RhNPs-MSNs-COOH	130 ± 50	-19 ± 8	779 ± 71 [a]	17 [c]	2.4	0.469	16.1 ± 0.3	11.1 ± 0.2	0.44 ± 0.08	-
RhNPs-MSNs-Tf	150 ± 70	-9 ± 5	n.d.	negative [d]	n.d.	n.d.	30.0 ± 0.2	16.1 ± 0.3	2.9 ± 0.2	0.23 ± 0.06

Fig. 2. (a) ATR-FTIR spectra of RhNPs-MSNs, RhNPs-MSNs-COOH, and RhNPs-MSNs-Tf. The assignment of the main vibration bands is displayed, including bands due to physisorbed water (*). Inset: zoom of the spectra in the 1850–1400 cm^{-1} region. (b) Nitrogen adsorption/desorption isotherms of the three nanomaterials. Inset: pore diameter distributions calculated using the BJH method. (c) Physicochemical parameters of the synthesized nanosystems including hydrodynamic diameter (DLS, $n = 5$), ζ-potential (n = 5), textural parameters (specific surface area (S_{BET}), BET C constant, pore diameter (D_P) obtained by using the BJH method, total pore volume (V_T) at $P/P_0 = 0.90$, organic content ($n = 3$), and elemental (C, N, S) composition (n = 3). [a] Standard error of the linear regression used to fit the BET equation in the specific surface area data. [b] C value in the range $20 < C < 100$, optimal for mesoporous silica confirming a well-defined monolayer-multilayer transition and ensuring that the BET equation is physically applicable [c] C value in the range $2\ L < C < 20$, suggest low affinity of nitrogen molecules for the surface, consistent with the organic functionalization. [d] The BET model coud not be reliably applied to RhNPs-MSNs-Tf material due to pore blockage by macromolecular functionalization, resulting in adsorption levels below the instrument's sensitivity threshold for standard BET analysis. [e] Organic content (wt%) is determined from the TGA weight losses, excluding the weight loss due to the desorption of water (up to 150 °C) and further corrected by the weight loss of the remaining alkoxysilanes after the sol–gel reaction (surfactant extracted unmodified RhNPs-MSNs) ($n = 3$).

Nitrogen sorption isotherms (Fig. 2b) exhibited type IV BET profiles with no observable hysteresis loop for both RhNPs-MSNs and RhNPs-MSNs-COOH, indicative of cylindrical mesopores with uniform size distributions. A marked decrease in specific surface area upon Tf conjugation (Fig. 2c) suggested partial pore blockage by protein adsorption [25]. Capillary condensation steps between P/P_0 = 0.27–0.37 (RhNPs-MSNs) and 0.17–0.30 (RhNPs-MSNs-COOH) reflected the presence of open mesopores (Fig. 2b); the diminished inflection in the latter implied restricted accessibility, consistent with successful carboxylation. All samples exhibited a secondary increase in adsorption at P/P_0 above 0.9, attributed to interparticle condensation, which was excluded from pore volume calculations. The decrease in the BET C constant (Fig. 2c) from 66 (RhNPs-MSNs) to 17 (RhNPs-MSNs-COOH) is consistent with the reduction in surface polarity and the replacement of surface silanols with organic functional groups, further confirming the successful modification of the silica surface. In RhNPs-MSNs-Tf, the external surface is fully functionalized with bulky Tf macromolecules that sterically block the pore entrances since the analysis is performed on the material in solid state. Consequently, nitrogen molecules are unable to access the internal mesopore volume, leading to a negligible amount of adsorbed gas that falls below the reliable quantification limit for the BET model.

ζ-potential measurements (Figs. 2c and **S3g–i**) further supported surface modifications. The initial RhNPs-MSNs displayed a potential of −12 mV, due to partially deprotonated surface silanols ($pk_a \approx 6.8$). Carboxylation increased the negative charge to −19 mV, reflecting additional deprotonated —COOH groups ($pK_a \approx 5.0$). Carboxylation increased the negative charge to −19 mV, due to the co-existence of the negative-charged -SiO^- groups of silica in water plus —COO^- groups from the new carboxylic acid functionalities. After Tf anchoring, ζ-potential increased to −9 mV, due to partial consumption of carboxylic groups during amide bonds formation.

Thermogravimetric (TGA) and elemental analyses supported the stepwise increase in organic content (Fig. 2c). MSNs-RhNPs, showed 6% organic material, attributed to residual ethoxy groups from incomplete TEOS hydrolysis and condensation. The %N in the RhNPs-MSNs material is due to the use of PVP as stabilizer during the synthesis of RhNPs. In RhNPs-MSNs-Tf, %N and %S increased significantly, with sulfur being detected exclusively in this final material, which is consistent with the amino acid composition of Tf (cysteine and methionine residues) and therefore confirms its successful conjugation.

3.2. *Photodynamic activity of RhNPs-MSNs-Tf nanophotosensitizer*

To evaluate the therapeutic potential of the RhNPs-MSNs-Tf nanosystem as a third-generation nanophotosensitizer, we next assessed its capacity to generate singlet oxygen ($^1O_2$) upon near-infrared (NIR) irradiation.

We used 1,3-diphenylisobenzofuran (DPBF) as a singlet oxygen molecular probe. DPBF undergoes rapid oxidation in the presence of

$^1O_2$, leading to a measurable decrease in its absorbance at 415 nm, a signal attributable solely to the reduced form of the probe. Thus, the rate of absorbance decay serves as an indirect quantification of $^1O_2$ production.

As shown in Fig. 3a, irradiation of RhNPs-MSNs-Tf at 800 nm led to a marked decrease in the DPBF absorbance signal, confirming the photodynamic activity of the nanomaterial under NIR excitation. These results demonstrate that RhNPs retain their photoactive properties following encapsulation within the MSN matrix and bioconjugation with transferrin, validating the functional integrity of the final nanophotosensitizer.

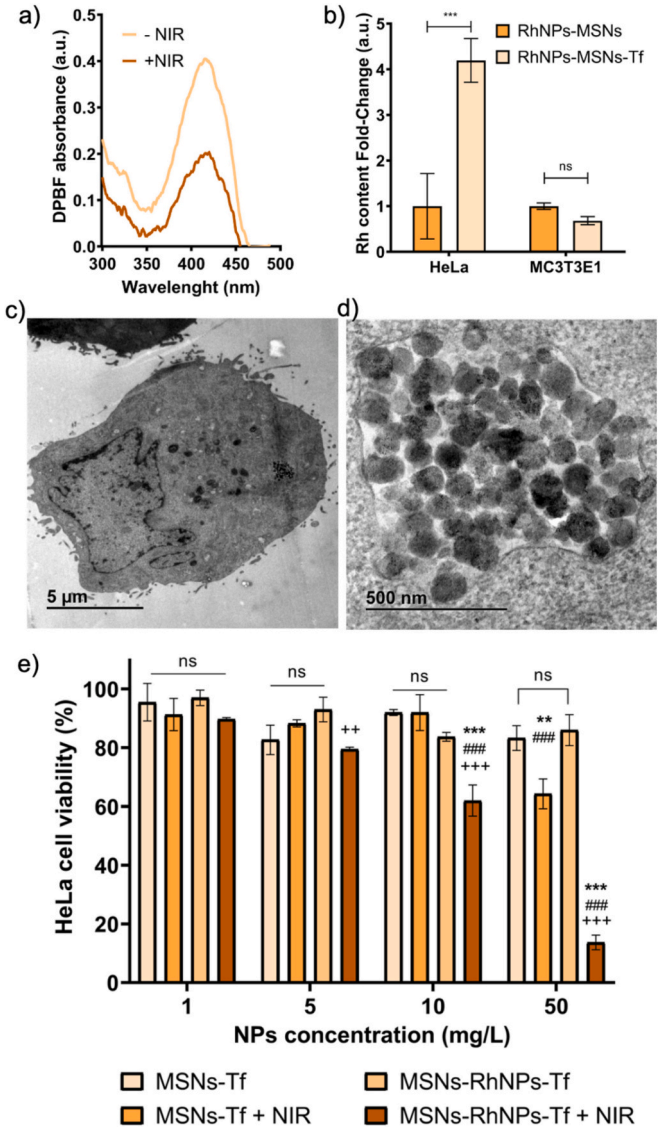

Fig. 3. (a) Decrease in absorbance at 415 nm of 1,3-diphenylisobenzofuran (DPBF) in the presence of RhNPs-MSNs-Tf under 800 nm irradiation, indicating singlet oxygen generation. (b) Total rhodium content in HeLa and MC3T3-E1 cells after 24 h exposure to RhNPs-MSNs-Tf or non-targeted RhNPs-MSNs (20 mg L^{-1}), determined by ICP-MS ($n = 5$). (c) Representative TEM micrograph of a HeLa cell following 24 h incubation with RhNPs-MSNs-Tf (20 mg L^{-1}), showing intracellular nanoparticle localization. (d) High-magnification TEM micrograph of an endosome containing internalized RhNPs-MSNs-Tf. (e) Viability of HeLa cells treated with MSNs-Tf or RhNPs-MSNs-Tf, with or without NIR irradiation, assessed by trypan blue exclusion assay (n = 5). Statistical analysis: one-way ANOVA with multiple comparisons. *ns*, not significant; ** $P < 0.01$, *** $p < 0.001$ versus MSNs-Tf. $^{\#\#}$ $p < 0.01$, $^{\#\#\#}$ $p < 0.001$ versus RhNPs-MSNs-Tf. $^{++}$ $p < 0.01$, $^{+++}$ $p < 0.001$ versus MSNs-Tf + NIR. (For interpretation of the references to colour in this figure legend, the reader is referred to the web version of this article.)

3.3. Targeting performance and intracellular localization of RhNPs-MSNs-Tf

To evaluate the targeting efficiency of the RhNPs-MSNs-Tf nanosystem toward transferrin receptor (TfR)-overexpressing cancer cells, we quantified rhodium uptake in cultured cells using inductively coupled plasma mass spectrometry (ICP-MS).

Two cell lines with contrasting levels of TfR expression were selected: HeLa cells (human cervical carcinoma), known to overexpress TfR, and MC3T3-E1 cells (mouse osteoblast-like), which exhibit basal TfR expression. As shown in Fig. 3b, rhodium accumulation in HeLa cells treated with RhNPs-MSNs-Tf was approximately four times higher as compared to cells treated with the protein-free non-targeted counterpart (RhNPs-MSNs), indicating enhanced cellular uptake mediated by transferrin conjugation. In contrast, MC3T3-E1 cells showed comparable rhodium levels regardless of the presence or absence of transferrin on the nanosystem, suggesting that internalization in these cells is not mediated by TfR. These results confirm that RhNPs-MSNs-Tf selectively targets TfR-overexpressing cells, potentially improving the tumor selectivity of the photodynamic therapy.

To further investigate the intracellular fate of the nanomaterial, we performed TEM analysis of HeLa cells following incubation with RhNPs-MSNs-Tf. As illustrated in **Fig. 3c** and **d**, a substantial number of nanoparticles were observed within intracellular vesicles consistent with endosomes. No particles were detected in the nucleus, which is in line with the ~100 nm size of the nanosystem and the size exclusion properties of the nuclear envelope.

3.4. Biocompatibility and photodynamic therapy efficacy of RhNPs-MSNs-Tf in cell culture

We assessed the cytotoxicity and photodynamic efficacy of the RhNPs-MSNs-Tf nanosystem in HeLa cells by performing a trypan blue exclusion assay under four experimental conditions. These were designed to isolate the specific contribution of each component: vehicle control (MSNs-Tf), complete nanosystem (RhNPs-MSNs-Tf), each tested with and without NIR irradiation across a concentration range of 1–50 mg L^{-1}.

In the absence of NIR irradiation, both MSNs-Tf and RhNPs-MSNs-Tf exhibited negligible cytotoxicity at all tested concentrations (Fig. 3e), confirming the intrinsic biocompatibility of the silica-based carrier and the RhNP-loaded system. These findings validate the suitability of the MSNs-Tf platform as a non-toxic delivery vehicle under dark conditions.

Upon NIR exposure, cells treated with MSNs-Tf maintained high viability up to 10 mg L^{-1}, consistent with the absence of intrinsic photodynamic activity of the silica-based vehicle [39–41]. Direct evaluation of intracellular reactive oxygen species (ROS) generation confirmed that MSNs-Tf does not induce ROS production under NIR irradiation (**Fig. S5**), supporting the lack of singlet oxygen generation by the silica matrix.

At the highest concentration tested (50 mg L^{-1}), a moderate decrease in cell viability was observed following NIR exposure. Given the absence of ROS generation (**Fig. S5**), this effect may be attributed to a concentration-dependent, nonspecific cellular stress response resulting from the combined presence of a high nanoparticle burden and irradiation, rather than to a photodynamic mechanism. Importantly, such an effect was not observed at concentrations used in subsequent mechanistic and in vivo experiments.

In contrast, HeLa cells treated with RhNPs-MSNs-Tf under NIR irradiation exhibited a pronounced, dose-dependent loss of viability. A significant photodynamic response was observed at concentrations above 10 mg L^{-1}, with cell viability decreasing to approximately 14% at 50 mg L^{-1}, clearly demonstrating that the therapeutic effect is

specifically mediated by rhodium nanoparticles.

These results confirm that cytotoxicity is specifically triggered by the combination of RhNPs and NIR irradiation, consistent with photodynamically generated singlet oxygen as the primary mechanism of action. Altogether, this demonstrates the therapeutic potential of RhNPs-MSNs-Tf as a light-activated, tumor-targeted nanophotosensitizer for cancer photodynamic therapy.

3.5. Mechanistic insights into RhNPs-MSNs-Tf photodynamic therapy via untargeted metabolomics

Understanding the biomolecular mechanisms underlying the therapeutic efficacy of novel photodynamic agents is essential for their rational development. To this end, we employed a GC–MS-based untargeted metabolomics approach (Fig. 4a) to investigate global metabolic alterations induced by RhNPs-MSNs-Tf-mediated photodynamic therapy (PDT) in HeLa cells.

Untargeted analysis identified 38 metabolites across treatment groups (**Table S1**). Principal component analysis (PCA) revealed a clear separation between control and treated samples at the 95% confidence level (Fig. 4b), with treated samples exhibiting positive PC1 scores, while controls showed negative PC1 values (Fig. 4c). Together, PC1 and PC2 accounted for 48.5% of total variance. The corresponding heatmap (Fig. 4d) further confirmed distinct metabolic fingerprints between treated and untreated cells. These data suggest that RhNPs-MSNs-Tf-mediated PDT induces specific metabolic responses in cancer cells. A Student's *t*-test ($p < 0.05$) identified 19 metabolites with significant abundance changes following PDT (**Table S2**). KEGG pathway enrichment analysis was performed using MetaboAnalyst 6.0 tool (**Fig. S6**) showing that the most prominently altered metabolites were associated with energy metabolism and reactive oxygen species (ROS)-related pathways such as dicarboxylate metabolism, unsaturated fatty acid biosynthesis, amino acid metabolism and glycolysis among others (Fig. 4e, f), pointing to a complex cellular response involving both metabolic reprogramming and oxidative stress.

A hallmark of cancer biology is metabolic reprogramming, with cancer cells exhibiting altered energy metabolism to support their rapid proliferation [42–44]. One of the best-known metabolic adaptations is the preference for aerobic glycolysis over mitochondrial oxidative phosphorylation, a phenomenon known as the Warburg effect [45]. Previous studies have shown that Rh-based compounds can interfere with cellular metabolism, and our findings suggest that RhNPs-MSNs-Tf induces similar effects by perturbing key metabolic intermediates (Fig. 4f).

In our system, aerobic glycolysis leads to pyruvate production via substrate-level phosphorylation, which is then converted to lactate (Rm = 0.56). Lactate excretion promotes acidification of the tumor microenvironment, facilitating angiogenesis, drug resistance, invasion, and metastasis [46,47]. In parallel, elevated levels of D-mannose (Rm = 1.87), a known disruptor of glycolytic flux that arrests the cell cycle [48], suggest interference with glucose metabolism. Increased acetate levels (Rm = 1.62) point to enhanced conversion of pyruvate into acetyl-CoA or increased fatty acid oxidation. This interpretation is supported by the reduced abundance of several fatty acids such as palmitate (Rm = 0.55) and stearate (Rm = 0.61), along with monoglycerides including monomyristin (Rm = 0.62), monopalmitin (Rm = 0.58), and monostearin (Rm = 0.59). These findings indicate that fatty acid β-oxidation may be acting as a compensatory energy source following inhibition of glycolysis (Fig. 5).

Paradoxically, de novo lipogenesis is also a metabolic hallmark of cancer, supporting membrane biosynthesis and cell division [49]. The photodynamic treatment mediated by RhNPs-MSNs-Tf appears to disrupt this balance by impairing glycolysis and forcing a shift toward catabolic lipid metabolism, thereby inducing metabolic stress in tumor cells.

This reprogramming is further supported by alterations in additional key metabolites. Phosphate (Rm = 0.62), frequently elevated in cancer cells due to its role in growth-promoting signaling cascades [50,51], was significantly reduced following PDT. Similarly, cholesterol (Rm = 0.57), essential for membrane integrity and implicated in tumor progression [52], was also downregulated, suggesting impaired cell proliferation capacity.

In addition to metabolic disruption, RhNPs-MSNs-Tf treatment was associated with oxidative stress. This is consistent with the production of singlet oxygen upon NIR irradiation, as demonstrated by DPBF assays. Metabolomic evidence includes the increased abundance of L-5-oxoproline (Rm = 1.78), a ROS-related intermediate of the γ-glutamyl cycle involved in glutathione metabolism [53,54]. Glutathione is a key cellular antioxidant, and perturbations in its synthesis pathway can sensitize cells to oxidative damage. Elevated levels of L-5-oxoproline, together with altered concentrations of amino acids such as L-serine (Rm = 1.80) and *L*-phenylalanine (Rm = 14.11), suggest glutathione imbalance and heightened susceptibility to oxidative stress (Fig. 5) [55,56].

Altogether, these results demonstrate that the therapeutic effects of RhNPs-MSNs-Tf-mediated PDT arise from a dual mechanism: disruption of tumor cell energy metabolism and induction of oxidative stress. This mechanistic insight provides a strong rationale for the further development of RhNPs-MSNs-Tf as a targeted nanophotosensitizer for cancer therapy.

3.6. In vivo evaluation of RhNPs-MSNs-Tf-mediated photodynamic therapy using the CAM model

While in vitro assays provided strong evidence for the targeted delivery and therapeutic efficacy of RhNPs-MSNs-Tf, cell culture models fail to capture the full biological complexity of living organisms. To bridge this gap and assess the translational potential of our nanophotosensitizer, we employed the chorioallantoic membrane (CAM) assay, an established and ethically favorable in vivo model that enables the study of tumor growth and therapeutic interventions in a vascularized environment [57–59].

For this experiment (Fig. 6a), we selected T47D human breast cancer cells, known for their reliable tumor engraftment in the CAM system [60]. Prior to the in vivo testing, we confirmed that RhNPs-MSNs-Tf induced a photodynamic effect in T47D cells in vitro, as demonstrated by reduced viability upon NIR irradiation in a trypan blue exclusion assay (Fig. 6b), in agreement with results obtained in HeLa cells.

Fertilized eggs were divided into four treatment groups: untreated controls, NIR irradiation alone (phototoxicity control), RhNPs-MSNs-Tf alone (nanomaterial toxicity control), and RhNPs-MSNs-Tf combined with NIR irradiation (therapeutic group).

On day 17 of embryo development, tumors were excised and analyzed (Fig. 6c). No significant differences in tumor mass were observed in the NIR-only or RhNPs-MSNs-Tf-only groups compared to controls, confirming the excellent biocompatibility and safety profile of both components individually. In contrast, embryos treated with the combination of RhNPs-MSNs-Tf and NIR exhibited a marked reduction in tumor weight (Fig. 6d), clearly demonstrating the therapeutic efficacy of the photodynamic treatment in vivo.

These results validate the antitumor potential of RhNPs-MSNs-Tf as a targeted, light-activated nanophotosensitizer, and establish a robust preclinical proof-of-concept for its future development as a third-generation platform for photodynamic cancer therapy.

4. Conclusions

In this work, we report the design and validation of RhNPs-MSNs-Tf, a third-generation nanophotosensitizer engineered for targeted photodynamic therapy under near-infrared (NIR) irradiation. By confining rhodium nanoparticles within mesoporous silica nanoparticles and functionalizing their surface with transferrin, we obtained a stable,

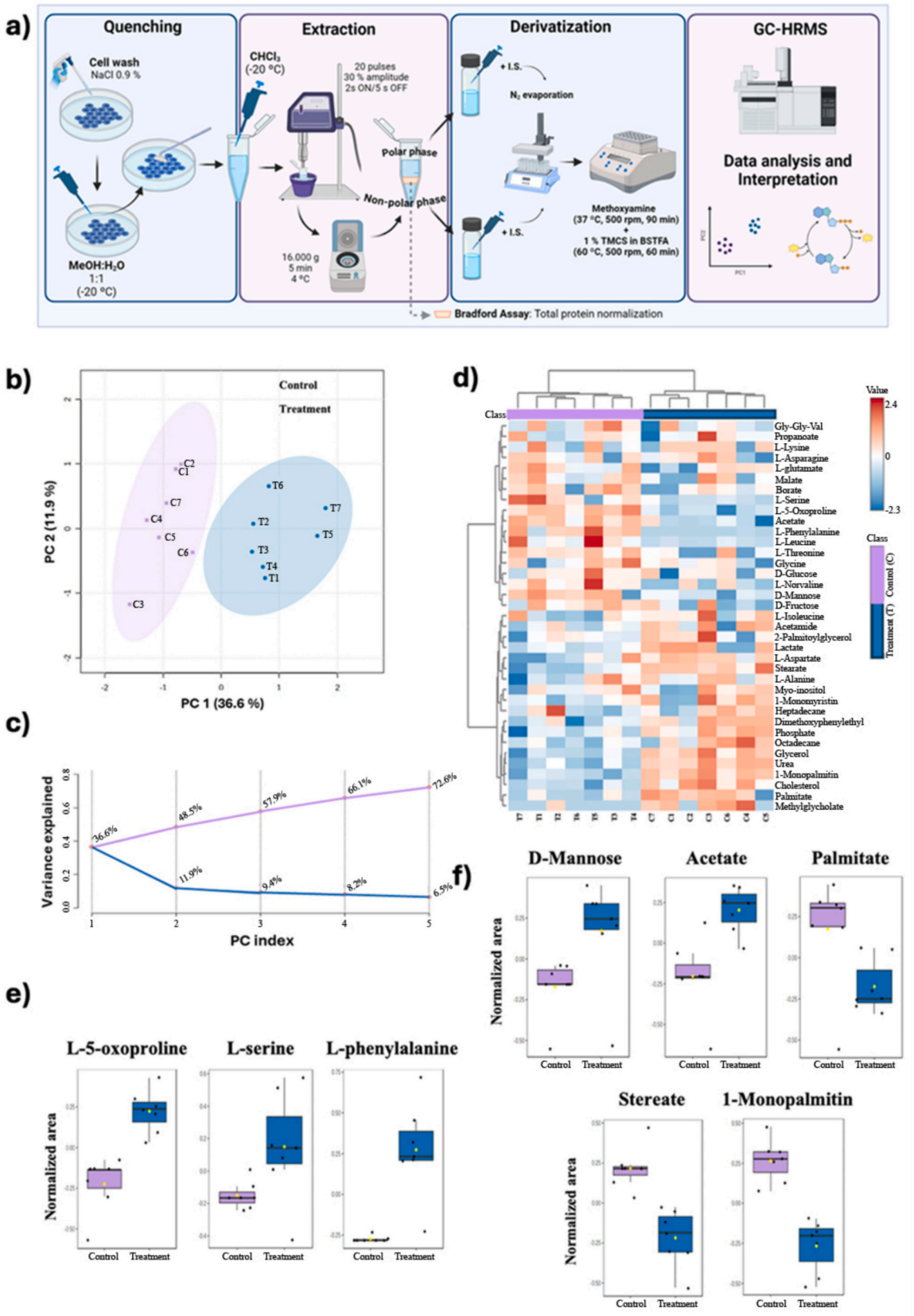

Fig. 4. Untargeted metabolomics analysis reveals metabolic alterations induced by RhNPs-MSNs-Tf-mediated photodynamic therapy ($n = 7$). a) Schematic overview of the experimental workflow for metabolite extraction and GC–MS-based untargeted analysis. b) Principal component analysis (PCA) scores plot showing clear separation between control and RhNPs-MSNs-Tf + NIR-treated samples. c) Explained variance for PC1 and PC2, accounting for 48.5% of the total variability. d) Heatmap of the 38 identified metabolites illustrating distinct metabolic fingerprints between conditions. e) Significantly altered metabolites associated with energy metabolism. f) Perturbation of metabolites linked to ROS generation and oxidative stress following treatment.

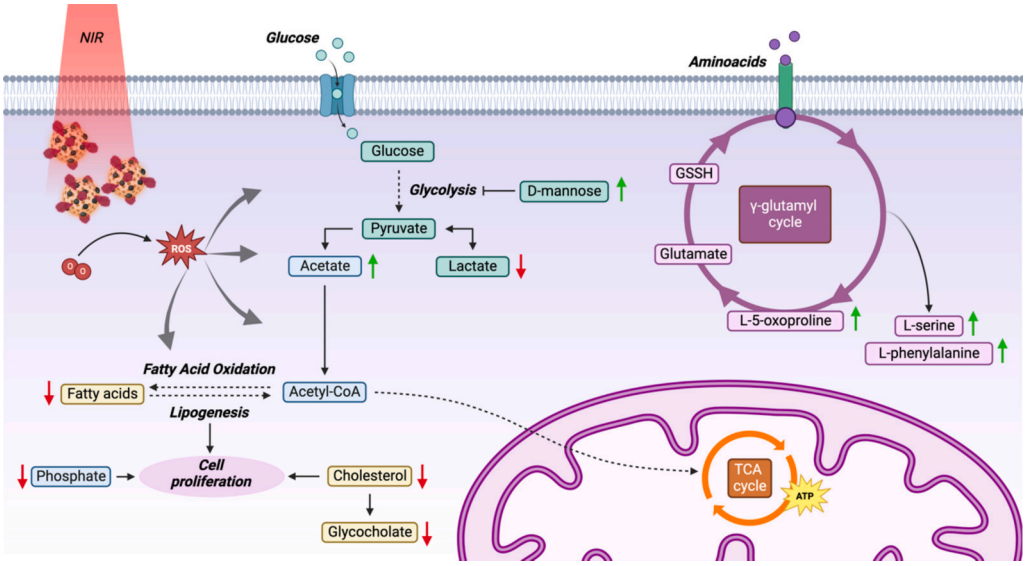

Fig. 5. Schematic representation of metabolic reprogramming induced by RhNPs-MSNs-Tf-mediated photodynamic therapy. The treatment disrupts aerobic glycolysis, leading to increased lactate production and acidification of the tumor microenvironment. Elevated levels of D-mannose indicate interference with glucose metabolism and cell cycle progression. Accumulation of acetate suggests enhanced fatty acid oxidation as a compensatory energy source in response to impaired glycolysis. Concurrent depletion of key lipids (e.g., palmitate, stearate, monoglycerides) and signaling molecules such as phosphate and cholesterol reflect broad metabolic disruption. Oxidative stress, triggered by singlet oxygen generation under NIR irradiation, results in elevated L-5-oxoproline, implicating glutathione cycle dysregulation and increased vulnerability of tumor cells to ROS-mediated cytotoxicity.

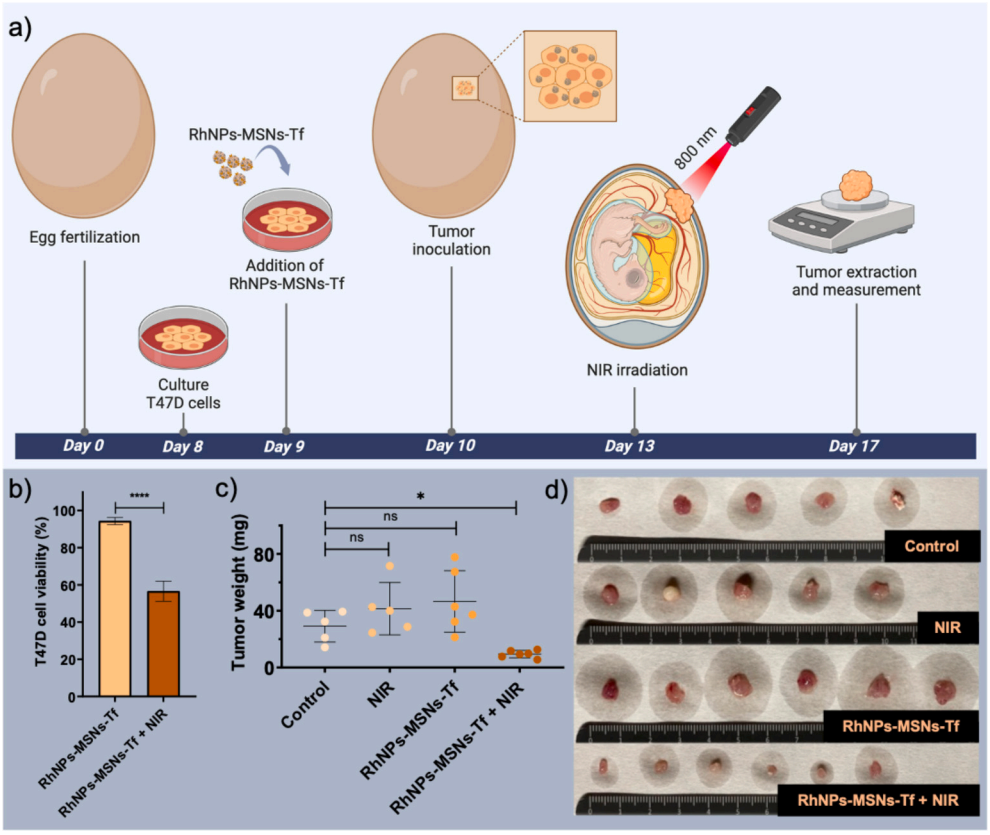

Fig. 6. In vivo assessment of RhNPs-MSNs-Tf-mediated photodynamic therapy using the CAM model. (a) Schematic representation of experimental design. Fertilized chicken eggs were divided into four groups: (1) untreated controls ($n = 5$), (2) NIR irradiation alone (n = 5), (3) RhNPs-MSNs-Tf alone ($n = 6$), and (4) RhNPs-MSNs-Tf combined with NIR irradiation (n = 6). (b) In vitro validation of photodynamic activity in T47D breast cancer cells treated with RhNPs-MSNs-Tf, with or without NIR exposure, using a trypan blue exclusion assay (n = 5). (c, d) Tumor weight measurements at day 17. No significant changes were observed in the NIR-only or RhNPs-MSNs-Tf-only groups. In contrast, combined treatment with RhNPs-MSNs-Tf and NIR irradiation resulted in a significant reduction in tumor mass. (For interpretation of the references to colour in this figure legend, the reader is referred to the web version of this article.)

biocompatible and actively targeted nanosystem capable of generating singlet oxygen upon NIR activation. The platform demonstrated selective uptake and light-triggered cytotoxicity in transferrin receptor-overexpressing cancer cells, together with significant tumor growth inhibition in the CAM model, while showing negligible toxicity in the absence of irradiation.

Beyond the development of a new nanomaterial, this study introduces the concept of metallic rhodium nanoparticles acting as intrinsic NIR-responsive photosensitizers whose biological activity can be mechanistically explained at the metabolic level. Unlike conventional organic or coordination-based photosensitizers, RhNPs combine photodynamic activity, high photostability and structural robustness, enabling their integration into multifunctional nanoplatforms. Importantly, the incorporation of untargeted metabolomics provides a systems-level understanding of PDT-induced cell death, revealing coordinated disruption of energy metabolism and redox homeostasis as key drivers of therapeutic efficacy.

Compared to previously reported nanophotosensitizers, which often focus primarily on ROS generation or in vitro cytotoxicity, RhNPs-MSNs-Tf integrates three key advances: (i) the use of metallic rhodium nanoparticles as NIR-activated photosensitizers, expanding the palette of inorganic PDT agents beyond conventional porphyrins or plasmonic systems; (ii) active tumor targeting through transferrin conjugation, enhancing selective cellular uptake; and (iii) mechanistic validation through metabolomics-based pathway analysis, which is rarely addressed in nanomedicine-driven PDT studies. These combined features position the present system beyond incremental material development and toward a mechanistically informed therapeutic platform [61,62].

Looking forward, this work opens several avenues for further development, including optimization of rhodium loading and particle architecture to fine-tune photodynamic efficiency, extension to deeper and more complex in vivo tumor models, and combination with metabolic or immunomodulatory therapies. More broadly, the strategy presented here establishes metallic rhodium-based nanocomposites as a versatile and previously unexplored class of functional materials for precision photodynamic therapy, with potential impact beyond oncology.

CRediT authorship contribution statement

Andres Machuca: Writing – original draft, Methodology, Investigation, Formal analysis, Data curation. **Roberto Alvarez-Fernandez Garcia:** Writing – original draft, Methodology, Investigation. **Alejandro Garcia-Garcia:** Methodology, Investigation. **Guillermo Aragoneses-Cazorla:** Methodology, Investigation. **Sonia Castillo-Lluva:** Supervision, Conceptualization. **Maria Vallet-Regi:** Writing – review & editing, Supervision. **Blanca González:** Writing – review & editing, Supervision, Formal analysis, Conceptualization, Funding acquisition. **Estefania Garcia-Calvo:** Writing – review & editing, Supervision, Formal analysis, Data curation, Conceptualization. **Jose L. Luque-Garcia:** Writing – review & editing, Supervision, Project administration, Funding acquisition, Formal analysis, Conceptualization.

Declaration of competing interest

The authors declare that they have no known competing financial interests or personal relationships that could have appeared to influence the work reported in this paper.

Acknowledgements

This work was supported by Ministerio de Ciencia, Innovación y Universidades grant PID2023-150182OB-I00. A.M. thanks Complutense University of Madrid and Banco Santander for the predoctoral grant CT82/20-CT83/20.

Appendix A. Supplementary data

Supplementary data to this article can be found online at https://doi.org/10.1016/j.jcis.2026.140143.

Data availability

Data will be made available on request.

References

[1] S. Kwiatkowski, B. Knap, D. Przystupski, J. Saczko, E. Kędzierska, K. Knap-Czop, J. Kotlińska, O. Michel, K. Kotowski, J. Kulbacka, Photodynamic therapy - mechanisms, photosensitizers and combinations, Biomed. Pharmacother. 106 (2018) 1098–1107.
[2] D. Dolmans, D.K. Fukumura, R. Jain, Photodynamic therapy for cancer, Nat. Rev. Cancer 3 (2003) 380–387.
[3] A.M. Rkein, D.M. Ozog, Photodynamic therapy, Dermatol. Clin. 32 (2014) 415–425.
[4] J.H. Correia, J.A. Rodrigues, S. Pimenta, T. Dong, Z. Yang, Photodynamic therapy review: principles, photosensitizers, applications, and future directions, Pharmaceutics 13 (2021) 1332.
[5] K. Furuse, M. Fukuoka, H. Kato, T. Horai, K. Kubota, N. Kodama, Y. Kusunoki, N. Takifuji, T. Okunaka, C. Konaka, A prospective phase II study on photodynamic therapy with photofrin II for centrally located early-stage lung cancer, J. Clin. Oncol. 11 (1993) 1852–1857.
[6] A.E. O'Connor, W.M. Gallagher, A.T. Byrne, Porphyrin and nonporphyrin photosensitizers in oncology: preclinical and clinical advances in photodynamic therapy, Photochem. Photobiol. 85 (2009) 1053–1074.
[7] T. Kormeili, P.S. Yamauchi, N.J. Lowe, Topical photodynamic therapy in clinical dermatology, Br. J. Dermatol. 150 (2004) 1061–1069.
[8] J.E. Blume, A.R., Oseroff, Aminolevulinic acid photodynamic therapy for skin cancers, Dermatol. Clin. 25 (2007) 5–14.
[9] M. Tavakkoli Yaraki, B. Liu, Y.N., Tan, emerging strategies in enhancing singlet oxygen generation of nano-photosensitizers toward advanced phototherapy, Nano Micro Lett. 14 (2022) 123.
[10] J. Chen, T. Fan, Z. Xie, Q. Zeng, P. Xue, T. Zheng, Y. Chen, X. Luo, H. Zhang, Advances in nanomaterials for photodynamic therapy applications: status and challenges, Biomaterials 237 (2020) 119827.
[11] M.R. Younis, G. He, J. Qu, P. Huang, X.H. Xia, Inorganic nanomaterials with intrinsic singlet oxygen generation for photodynamic therapy, Adv. Sci. 8 (2021) 2102587.
[12] S.S. Lucky, K.C. Soo, Y. Zhang, Nanoparticles in photodynamic therapy, Chem. Rev. 115 (2015) 1990–2042.
[13] A. Serrano-Maldonado, S.S. Rozenel, J.L. Jimenez-Santiago, I. Guerrero-Ríos, E. Martin, Rh nanoparticles from thiolate dimers: selective and reusable hydrogenation catalysts in ionic liquids, Catal. Sci. Technol. 8 (2018) 4373–4382.
[14] M.J. Jacinto, P.K. Kiyohara, S.H. Masunaga, R.F. Jardim, L.M. Rossi, Recoverable rhodium nanoparticles: synthesis, characterization and catalytic performance in hydrogenation reactions, Appl. Catal. A 338 (2008) 52–57.
[15] M. Gulcan, Y. Karata, Synthesized polyvidone-stabilized Rh(0) nanoparticles catalyzed the hydrolytic dehydrogenation of methylamine-borane in ambient conditions, New J. Chem. 41 (2017) 11839–11845.
[16] S. Czerczak, J.P. Gromiec, A. Pałaszewska-Tkacz, Patty's Toxicology, Wiley, 2012. Ch. 19.
[17] C. Pérez-Arnaiz, M. Acuña, N. Busto, I. Echevarría, M. Martínez-Alonso, G. Espino, B. García, F. Domínguez, Thiabendazole-based Rh(III) and Ir(III) biscyclometallated complexes with mitochondria-targeted anticancer activity and metal-sensitive photodynamic activity, Eur. J. Med. Chem. 157 (2018) 279–293.
[18] B. Zhang, J. Xiao, X. Wang, P. Li, W. Su, Synthesis, characterization and photodynamic activity of half-sandwich rhodium(III) complexes with curcuminoids, Photodiagn. Photodyn. Ther. 32 (2020) 102049.
[19] S. Kang, W. Shin, M. Choi, M. Ahn, Y. Kim, S. Kim, D. Min, H. Jang, Morphology-controlled synthesis of rhodium nanoparticles for cancer phototherapy, ACS Nano 12 (2018) 6997–7008.
[20] H. Wang, H. Wang, G. Yu, L. Xie, C. Zhang, C. Xu, X. Ma, Z. Miao, Y. Yu, Naked mesoporous rhodium nanospheres with glutathione depletion and photothermal capabilities for tumor therapy, J. Colloid Interface Sci. 677 (2025) 1075–1083.
[21] A. Machuca, E. Garcia-Calvo, D.S. Anunciação, J.L. Luque-Garcia, Rhodium nanoparticles as a novel photosensitizing agent in photodynamic therapy against cancer, Chem. Eur. J. 26 (2020) 7685–7691.
[22] A. Machuca, E. Garcia-Calvo, D.S. Anunciação, J.L. Luque-Garcia, Integration of transcriptomics and metabolomics to reveal the molecular mechanisms underlying rhodium nanoparticles-based photodynamic cancer therapy, Pharmaceutics 13 (2021) 1629.
[23] M. Vallet-Regí, F. Schüth, D. Lozano, M. Colilla, M. Manzano, Engineering mesoporous silica nanoparticles for drug delivery: where are we after two decades? Chem. Soc. Rev. 51 (2022) 5365.
[24] B. Xu, S. Li, R. Shi, H. Liu, Multifunctional mesoporous silica nanoparticles for biomedical applications, Signal Transduct. Target. Ther. 8 (2023) 435.
[25] S. Montalvo-Quiros, G. Aragoneses-Cazorla, L. Garcia-Alcalde, M. Vallet-Regí, B. González, J.L. Luque-García, Cancer cell targeting and therapeutic delivery of

silver nanoparticles by mesoporous silica nanocarriers: insights into the action mechanisms using quantitative proteomics, Nanoscale 11 (2019) 4531–4545.
[26] S. Montalvo-Quirós, S. Gómez-Graña, M. Vallet-Regí, R. Prados-Rosales, B. González, J.L. Luque-García, Mesoporous silica nanoparticles containing silver as novel antimycobacterial agents against mycobacterium tuberculosis, Colloids Surf. B: Biointerfaces 197 (2021) 111405.
[27] G. Aragoneses-Cazorla, J. Serrano-Lopez, I. Martinez-Alfonzo, M. Vallet-Regí, B. González, J.L. Luque-Garcia, A novel hemocompatible core@shell nanosystem for selective targeting and apoptosis induction in cancer cells, Inorg. Chem. Front. 8 (2021) 2697–2712.
[28] A. García, B. González, C. Harvey, I. Izquierdo-Barba, M. Vallet-Regí, Effective reduction of biofilm through photothermal therapy by gold core@shell based mesoporous silica nanoparticles, Microporous Mesoporous Mater. 328 (2021) 111489.
[29] F. Rizzi, E. Fanizza, M. Giancaspro, N. Depalo, M.L. Curri, B. González, M. Colilla, I. Izquierdo-Barba, M. Vallet-Regí, Mesoporous silica nanostructures embedding NIR active plasmonic nanoparticles: harnessing antimicrobial agents delivery system for photo-assisted eradicating gram-positive bacteria, Microporous Mesoporous Mater. 383 (2025) 113414.
[30] K.R. Kampen, Membrane proteins: the key players of a cancer cell, J. Membr. Biol. 242 (2011) 69–74.
[31] S. Takaishi, T. Okumura, S. Wang, W. Shibata, R. Vigneshwaran, S.A.K. Gordon, Y. Shimada, T.C. Wang, Identification of gastric cancer stem cells using the cell surface marker CD44, Stem Cells 27 (2009) 1006–1020.
[32] G. Leon, L. MacDonagh, S.P. Finn, S. Cuffe, M.P. Barr, Cancer stem cells in drug resistant lung cancer: targeting cell surface markers and signaling pathways, Pharmacol. Ther. 158 (2016) 71–90.
[33] W. Wang, Z. Deng, H. Hatcher, L. Miller, X. Di, L. Tesfay, G. Sui, R. D'Agostino, F. Torti, S. Torti, IRP2 regulates breast tumor growth, Cancer Res. 74 (2014) 497–507.
[34] J.D. Hoefelmeyer, K. Niesz, G.A. Somorjai, T.D. Tilley, Radial anisotropic growth of rhodium nanoparticles, Nano Lett. 5 (2005) 435–438.
[35] L. Xu, D. Liu, D. Chen, H. Liu, J. Yang, Size and shape controlled synthesis of rhodium nanoparticles, Heliyon 5 (2019) e01165.
[36] Á. Martínez, E. Fuentes-Paniagua, A. Baeza, J. Sánchez-Nieves, M. Cicuéndez, M. Gómez, F.J. De La Mata, B. González, M. Vallet-Regí, Mesoporous silica nanoparticles decorated with carbosilane dendrons as new non-viral oligonucleotide delivery carriers, Chem. Eur. J. 21 (2015) 15651–15666.
[37] F. Rizzi, R. Castaldo, T. Latronico, P. Lasala, G. Gentile, M. Lavorgna, M. Striccoli, A. Agostiano, R. Comparelli, N. Depalo, M.L. Curri, E. Fanizza, High surface area mesoporous silica nanoparticles with tunable size in the sub-micrometer regime: insights on the size and porosity control mechanisms, Molecules 26 (2021) 4247.
[38] R. Ryoo, C.H. Ko, I.S. Park, Synthesis of highly ordered MCM-41 by micelle-packing control with mixed surfactants, Chem. Commun. 15 (1999) 1413–1414.
[39] J.K. Fu, Y. Wang, Y.C. Zhu, Broadband and high diffuse reflectivity of hollow-mesoporous silica nanospheres and their UV light shielding ability for light-labile peroxides, Mater. Lett. 153 (2015) 89–91.
[40] A. Usami, Theoretical simulations of optical confinement in dye-sensitized nanocrystallilne solar cells, Sol. Energy Mater. Sol. 64 (2000) 73–83.
[41] J. Fina, N. Kaur, C.Y. Chang, C.Y. Lai, D.R. Radu, Enhancing light harvesting in dye-sensitized solar cells through mesoporous silica nanoparticle-mediated diffuse scattering back reflectors, Electron. Mater. 4 (2023) 124–135.
[42] R. Moreno-Sánchez, S. Rodríguez-Enríquez, A. Marín-Hernández, E. Saavedra, Energy metabolism in tumor cells, FEBS J. 274 (2007) 1393–1418.
[43] S. Romero-Garcia, J.S. Lopez-Gonzalez, J.L. Báez-Viveros, D. Aguilar-Cazares, H. Prado-Garcia, Tumor cell metabolism: an integral view, Cancer Biol. Ther. 12 (2011) 939–948.
[44] I. Martínez-Reyes, N.S. Chandel, Cancer metabolism: looking forward, Nat. Rev. Cancer 21 (2021) 669–680.
[45] M.V. Liberti, J.W. Locasale, The Warburg effect: how does it benefit cancer cells? Trends Biochem. Sci. 41 (2016) 211–218.
[46] Z. Li, Q. Wang, X. Huang, M. Yang, S. Zhou, Z. Li, Z. Fang, Y. Tang, Q. Chen, H. Hou, L. Li, F. Fei, Q. Wang, Y. Wu, A. Gong, Lactate in the tumor microenvironment: a rising star for targeted tumor therapy, Front. Nutr. 10 (2023) 1113739.
[47] M. Cai, J. Wan, K. Cai, H. Song, Y. Wang, W. Sun, J. Hu, Understanding the contribution of lactate metabolism in cancer progress: A perspective from isomers, Cancers 15 (2023) 10087.
[48] P.S. Gonzalez, J. O'Prey, S. Cardaci, V.J.A. Barthet, J.I. Sakamaki, F. Beaumatin, A. Roseweir, D.M. Gay, G. Mackay, G. Malviya, Mannose impairs tumour growth and enhances chemotherapy, Nature 563 (2018) 719–723.
[49] V. Chajès, M. Cambot, K. Moreau, G.M. Lenoir, V. Joulin, Acetyl-CoA carboxylase á is essential to breast cancer cell survival, Cancer Res. 66 (2006) 5287–5294.
[50] R.B. Brown, Obesity and cancer: potential mediation by dysregulated dietary phosphate, Obesities 2 (2022) 64–75.
[51] G. Chazot, S. Lemoine, G. Kocevar, E. Kalbacher, D. Sappey-Marinier, O. Rouvière, L. Juillard, Intracellular phosphate and ATP depletion measured by magnetic resonance spectroscopy in patients receiving maintenance hemodialysis, J. Am. Soc. Nephrol. 32 (2021) 229–237.
[52] X. Ding, W. Zhang, S. Li, H. Yang, The role of cholesterol metabolism in cancer, Am. J. Cancer Res. 9 (2019) 219–227.
[53] A. Van Der Pol, A. Gil, H.H.W. Silljé, J. Tromp, E.S. Ovchinnikova, I. Vreeswijk-Baudoin, M. Hoes, I.J. Domian, B. Van De Sluis, J.M. Van Deursen, A.A. Voors, D. J. Van Veldhuisen, W.H. Van Gilst, E. Berezikov, P. Van Der Harst, R.A. De Boer, R. Bischoff, P. Van Der Meer, Accumulation of 5-oxoproline in myocardial dysfunction and the protective effects of OPLAH, Sci. Transl. Med. 9 (2017) 415.
[54] A. Van der Pol, A. Gil, J. Tromp, H.H.W. Silljé, D.J. Van Veldhuisen, A.A. Voors, E. S. Hoendermis, N.G. Beverborg, E.M. Schouten, R.A. de Boer, R. Bischoff, P. Van der Meer, Death of an antioxidant brings heart failure with preserved ejection fraction to life: 5-oxoproline and post-ischaemic cardio-renal dysfunction, Cardiovasc. Res. 114 (2018) 1871–1882.
[55] Y. Gamarra, F.C. Santiago, J. Molina-López, J. Castaño, L. Herrera-Quintana, A. Domínguez, E. Planells, Pyroglutamic acidosis by glutathione regeneration blockage in critical patients with septic shock, Crit. Care 23 (2019) 162.
[56] D.H. Kwon, H.J. Cha, H. Lee, S.H. Hong, C. Park, S.H. Park, G.Y. Kim, S. Kim, H. S. Kim, H.J. Hwang, Y.H. Choi, Protective effect of glutathione against oxidative stress-induced cytotoxicity in RAW 264.7 macrophages through activating the nuclear factor erythroid 2-related factor-2/heme oxygenase-1 pathway, Antioxidants 8 (2019) 82.
[57] L. Miebach, J. Berner, S. Bekeschus, In ovo model in cancer research and tumor immunology, Front. Immunol. 13 (2022) 1006064.
[58] D. Ribatti, The chick embryo chorioallantoic membrane (CAM) assay, Reprod. Toxicol. 70 (2017) 97–101.
[59] D. Ribatti, The chick embryo chorioallantoic membrane (CAM). A multifaceted experimental model, Mech. Dev. 141 (2016) 70–77.
[60] A. Martowicz, G. Spizzo, G. Gastl, G. Untergasser, Phenotype-dependent effects of EpCAM expression on growth and invasion of human breast cancer cell lines, BMC Cancer 12 (2012) 501.
[61] R. Prieto-Montero, T. Arbeloa, V. Martinez-Martinez, Photosensitizer-mesoporous silica nanoparticles combination for enhanced photodynamic therapy, Photochem. Photobiol. 99 (2023) 882–900.
[62] L. Lin, X. Song, X. Dong, B. Li, Nano-photosensitizers for enhanced photodynamic therapy, Photodiagn. Photodyn. Ther. 36 (2021) 102597.